

ARTICLE OPEN



Research on the degradation of ancient Longquan celadons in the Dalian Island shipwreck

Yan He^{1,2,3,4}, Weidong Li^{1,2,3,4}✉, Jianan Li⁵, Changsong Xu^{1,2,3,4} and Xiaoke Lu^{1,2,3,4}

Eleven celadons with different degrees of degradation excavated from the Dalian Island shipwreck of the Yuan Dynasty (1271–1368 AD) were selected, and the degradation mechanism of the ancient porcelain at marine environment was investigated. The chemical composition, microstructure, and corrosion morphology of the samples were characterized. The results showed that these celadons can be divided into two types: transparent glazes and matt-opaque glazes. The glazes are subject to the combined effects of physical damage and chemical corrosion. The glaze surface became rougher through physical impact, and the increased surface area may also promote chemical corrosion. The mutual promotion of the two effects usually leads to more serious degradation. There are two possible corrosion mechanisms, depending on the glaze microstructure. Transparent glazes may experience the process of dissolution and reprecipitation. The crystallization-phase-separation structure in the matte glaze has lower chemical stability, which can contribute to more extensive corrosion.

npj Materials Degradation (2022)6:4; <https://doi.org/10.1038/s41529-022-00217-5>

INTRODUCTION

Degradation of materials is a ubiquitous yet harmful complex process, the rate and extent of degradation usually depend on the composition and microstructure of the material and environmental factors^{1–3}. Ancient cultural relic materials are no exception⁴, since they often undergo long burial periods prior to archeological excavations, lasting from hundreds to thousands of years. During this period, various physical and chemical interactions occur between these materials and the natural environment. The degradation process may be slow, but it is unavoidable^{5,6}.

Chinese porcelain has always been an important trade commodity on the ancient Maritime Silk Road, and a large number of ceramics have also been discovered in underwater archeology in recent years. These precious cultural heritages serve as evidence of human cultural exchanges and economic trade, as well as possess high historical, cultural, and research value. Although porcelains are generally considered to have good corrosion resistance and can be maintained for a long time, they often suffer various degrees of damage in harsh marine environments, such as contamination, lower gloss, surface roughening, flaking, crazing, and even breakage^{7–13}. Various diseases have severely damaged their exquisite appearance and have brought great challenges to the subsequent conservation. Common treatment methods include immersion in deionized water for desalination, and the use of chemical reagents to remove concretion^{5,9–11}. If not properly protected, it is easy to cause “secondary damage”^{14,15}. However, owing to the large amount of different porcelain wares, it is impossible to analyze each individually. Therefore, it is important to analyze conventional porcelain with damage. Not only can it provide information about the preservation conditions of excavated porcelain, but can also enhance the understanding of the degradation mechanism of porcelain in natural environments, providing a scientific basis for selecting suitable protection and treatment methods. Therefore, to carry out the protection and conservation of cultural relics

scientifically, it is essential to have an in-depth understanding of the properties of cultural relics themselves, the environment, and the interactions between them.

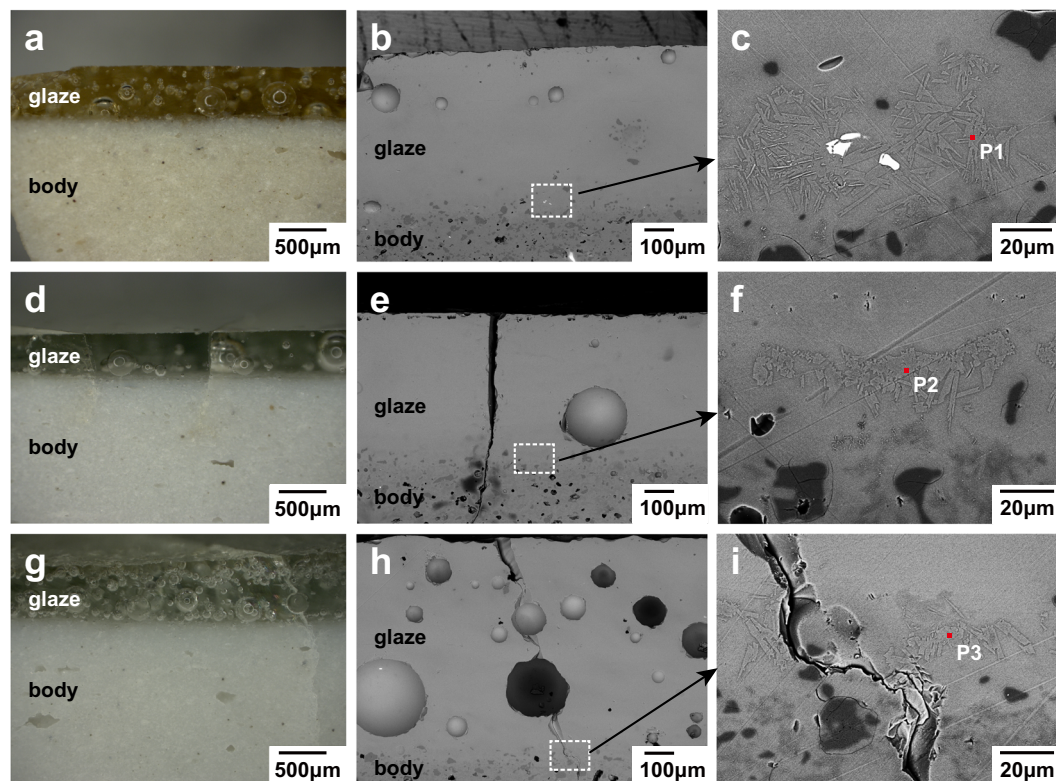
Porcelain comprises a ceramic body and a glaze, and most of the body is covered by glaze¹⁶. Glaze is a heterogeneous material. From the perspective of microstructure, glass phases, unmelted quartz grains from the raw material, crystallization, phase separation, and bubbles may coexist in the glaze¹⁶. In addition, there is an interaction layer at the glaze-body interface, resulting from component diffusion, which affects the composition of the thin glaze layer¹⁷. Therefore, it is difficult to analyze each phase or each microarea separately, which would greatly increase the complexity of the degradation mechanism. The chemical corrosion of the glass phase is often a concern because it is the main phase in the glaze. For instance, researchers have used infrared spectroscopy or Raman spectroscopy to study the alteration of silicon–oxygen tetrahedrons in ancient glaze under different solutions^{18,19}. A silicon-rich hydrated layer was detected on the glaze surface of ancient black-glazed porcelain, which was attributed to the interdiffusion reaction between the cations in the glaze and the hydrogenated species in the solution²⁰. Moreover, the wollastonite crystalline phases were found to be preferentially corroded than glass phase in Jun glaze, indicating the effect of heterogeneity on corrosion²¹. However, there is still a lack of comparative studies on the degradation of ancient glaze with different microstructures under the same conditions, which is required for a complete understanding of the underlying degradation mechanisms of ancient ceramics in marine environments. The batch of Longquan celadon wares from the Dalian Island shipwreck of the Yuan Dynasty provides an excellent opportunity for a case study.

The shipwreck was found in the area between Dalian Island and Xiaolian Island in Pingtan County, Fujian Province, China, at a depth of 15–18 m; the geographical position is shown in Supplementary Fig. 1. The sea area is located in a main maritime

¹Shanghai Institute of Ceramics, Chinese Academy of Sciences, Shanghai 201899, China. ²Key Scientific Research Base of Ancient Ceramics, State Administration for Cultural Heritage, Shanghai 201899, China. ³Key Laboratory of the Comprehensive Analysis Technology for Ancient Ceramics and its Applications, Ministry of Culture and Tourism, Shanghai 201899, China. ⁴University of Chinese Academy of Sciences, Beijing 100049, China. ⁵Fujian Museum, Fuzhou 350025, China. ✉email: liwd@mail.sic.ac.cn

Table 1. Chemical compositions of the glass phase acquired on the cross section of the glaze by EDS (in wt%).

Sample No.	Na ₂ O	MgO	Al ₂ O ₃	SiO ₂	K ₂ O	CaO	TiO ₂	Fe ₂ O ₃	P ₂ O ₅	MnO
01	<0.5	2	15	64	6	10	<0.5	1	1	1
02	1	1	16	68	7	5		1	1	<0.5
05	1	1	17	67	7	5		2	1	<0.5
06		1	15	64	5	13		2		<0.5
07	<0.5	1	14	62	5	15		2	<0.5	1
08	1	1	14	68	6	7		2	<0.5	1
09	1	3	16	60	5	15				
10	<0.5	1	15	65	7	9		2	<0.5	1

**Fig. 1** OM and SEM images of the polished cross section of Nos. 01, 02, and 05. a–c No. 01; d–f No. 02; g–i No. 05, where c, f, and i are the local magnified images of the glaze-body interface of Nos. 01, 02, and 05, respectively.

trade passage, known as the “sea corridor”, from which abundant underwater cultural heritage pieces have been excavated. The sunken shipwreck sites discovered cover various historical periods from the Five Dynasties (907–960 AD) to the Qing Dynasty (1636–1912 AD)²². After the discovery of the Dalian Island shipwreck during an archeological investigation along the coast of Fujian province in September 2006, a salvage underwater archeological excavation was carried out in October 2007 to avoid the theft of underwater cultural relics. Most of the excavated relics are ceramics, with a total of 603 pieces, mainly celadon wares, in the shape of bowls, large plates, washers, jarlets, etc., as well as potteries and an iron pot²². According to analyses by archeologists, all of these celadon wares were produced by Longquan kiln in Zhejiang province, possibly from the Longquan Dayao and Xikou kiln sites²². This batch of celadon wares from the same shipwreck showed significant differences in appearance and condition, which brought a special perspective to the research on degradation mechanisms. In this study, a representative group

of celadon wares, with varying degrees of degradation, were selected, and the underlying degradation processes were discussed from the perspectives of chemical composition, firing temperature, microstructure, and marine environment.

RESULTS AND DISCUSSION

Chemical compositions of the celadon bodies and glazes

Chemical compositions of the body and the glaze of the 11 samples are listed in Supplementary Table 1 and Table 1, respectively. The chemical compositions of the sample bodies are similar and are consistent with the compositions of the typical Longquan celadon bodies²³, indicating that the batch of celadon was likely produced in the same kiln. The composition acquired on the cross section of the glaze avoids corrosion of the surface, so it can generally represent the composition of the uncorroded glaze. For the transparent glaze, the compositions acquired on the glaze surface and cross section were not significantly different. In the

Table 2. Chemical compositions of the marked positions (crystalline phase) shown in Fig. 1, Fig. 6, Fig. 9, and Fig. 10 (in atom%).

Figures	Position	O	Na	Mg	Al	Si	K	Ca	Fe	Ti	P	Mn
Fig. 1	P1	62	<0.5		14	18	<0.5	6	<0.5			
	P2	62	1		15	17	<0.5	5			<0.5	
	P3	62	1		14	17	<0.5	6	<0.5			
Fig. 6	P1	62	1	<0.5	9	21	2	5	<0.5			<0.5
	P2	62	1	<0.5	13	17	1	6	<0.5			
Fig. 9	P1	60		8	2	19		9	1		1	<0.5
	P2	62	1	1	10	20	1	5	<0.5		<0.5	<0.5
	P3	62	1	<0.5	11	20	1	5	<0.5	<0.5	<0.5	
	P4	62	<0.5	1	4	15	2	10	<0.5		6	<0.5
Fig. 10	P1	62	1	<0.5	10	19	1	6	1			<0.5

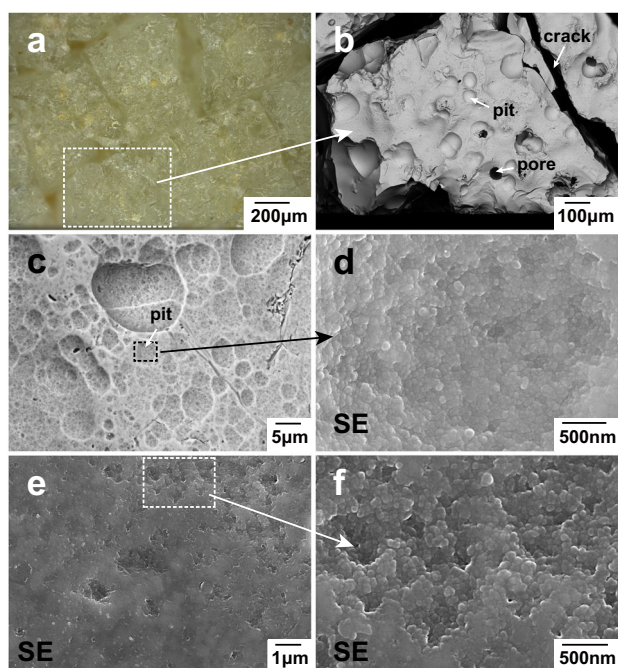


Fig. 2 OM and SEM images of sample No. 06. **a** and **b** are the OM and SEM images of the glaze surface, respectively; **c** SEM image of the hemispherical pits on the glaze surface: the rectangle region in **b**; **d** SEM image of the submicron spherical aggregates on the inner wall of a pit; **e** SEM image of the irregularly shaped pits on the glaze surface; **f** SEM image of the submicron spherical aggregates in the irregularly shaped pits; **b** and **c** are backscattered electron images, and **d–f** are secondary electron images.

matte glaze, the MgO content of the altered glaze surfaces of Nos. 08 (2.33 wt%) and 09 (16.31 wt%) was higher than that of the cross section (0.33 wt% and 1.26 wt%, respectively). The Fe₂O₃ content of the altered surface of No. 09 (9.78 wt%) was also significantly higher than that of the cross section (1.99 wt%). To show the difference in the glaze composition more intuitively, the analysis diagram of MgO and Fe₂O₃ contents is plotted, as shown in Supplementary Fig. 2. It is shown that the compositions acquired on the cross section and the altered surface of most samples are similar, while the contents of altered surface of Nos. 08 and 09 are significantly higher. For No. 08, the reason for the difference may be due to surface crystallization, while the greater difference of No. 09 may relate to the corrosion process and yellow substances on the surface, which will be further explained below by combining the glaze microstructure.

Well-preserved transparent glazes

Longquan celadon glaze during the Yuan Dynasty was mostly transparent glaze, with a relatively high firing temperature and a high degree of vitrification, in which there were few unmelted quartz grains and other crystals²³. Sample Nos. 01–07 were all covered with transparent glaze, including both well-preserved samples (Nos. 01–05) and partially corroded samples (Nos. 06 and 07). XRD (X-ray diffraction analysis) was first used to examine the crystalline phase on the glaze surface of Nos. 01, 02, and 05, and the results showed (Supplementary Fig. 3) that only diffraction peaks of quartz could be detected for No. 01, and the amorphous glass phase was the dominant phase across the three samples.

The OM (optical microscopy) and SEM (scanning electron microscopy) images of the polished cross section (Fig. 1) indicate that the glazes of Nos. 01, 02, and 05 are clear and transparent, with only a certain number of bubbles and few unmelted quartz grains (the Raman spectrum of the quartz grain is shown in Supplementary Fig. 4), which also supports the XRD analysis results. Many needle-like crystals ranging from a few microns to tens of microns in length are distributed at the glaze-body interface (Fig. 1c, f, and i), and the results of the EDS (energy-dispersive X-ray energy spectrometry) analysis (Table 2) and Raman spectra (Supplementary Fig. 5) indicate that they are anorthite crystals (CaAl₂Si₂O₈). For the glaze surfaces of Nos. 01, 02, and 05, some scratches and pits possibly caused by mechanical force can be found under OM, and no obvious corrosion traces are observed.

Transparent glazes with poor conditions

Nos. 06 and 07 were two corroded samples with a transparent glaze. There are no visible diffraction peaks of the crystalline phase in the XRD diagram acquired on the glaze surface of Nos. 06 and 07 (Supplementary Fig. 6), and only a broad peak of the glass phase was observed. The glaze surface of No. 06 is uneven and divided into several irregularly shaped areas by several cracks (widths of tens of microns, Fig. 2a and b). There are a large number of hemispherical pits on the glaze surface, approximately several microns to tens of microns in diameter (Fig. 2c). Further magnified images show that small spherical aggregates with a size of approximately tens of nanometers are distributed on the inner wall of the pits (Fig. 2d). Other surface regions without hemispherical pits are not smooth and flat, and there are many irregularly shaped pits with a large number of submicron spherical aggregates (Fig. 2e and f). These micron-sized pits may be formed by the physical impact of the sand particles in the seawater, and they significantly increased the roughness of the glaze surface. In addition, some smooth fractures left by the delamination of the glaze caused by mechanical forces were observed on the glaze surface.

A micro-Raman spectrometer was used to test multiple positions on the glaze surface of No. 06, including the inside and outside of the pits, and the typical results are shown in Fig. 3. Only the typical Raman band of glass was observed at 480 and 1020 cm^{-1} , corresponding to the bending and stretching vibrational modes of the Si–O bond of the SiO_4 tetrahedron²⁴. The deconvolution of the curves shows that the stretching bands are mainly determined by Q^2 component^{24,25}. This also indicates that there may be no neoformed crystalline phase at the measured positions, including inside the pits.

According to the results of XRD and Raman analysis, it can be concluded that the main phase of the transparent glaze is the aluminosilicate glass phase and that there are few other crystalline

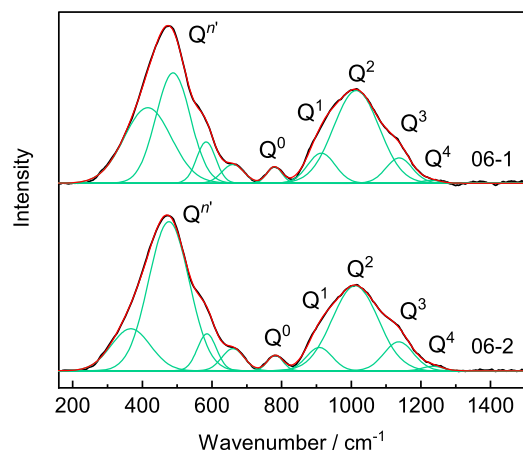


Fig. 3 Raman spectra of the glaze surface of sample No. 06. 06-1 and 06-2 were tested inside and outside the pits, respectively. The black, green, and red lines represent the original Raman spectral curve, the components of spectral curve, and the fitted spectral curve, respectively. Q^n ($n = 0, 1, 2, 3, 4$) and $Q^{n'}$ correspond to the stretching and bending vibrational modes of the Si–O bond of the SiO_4 tetrahedron.

phases in addition to a small number of unmelted quartz grains in the glaze. Generally, the chemical corrosion of silicate glass in aqueous solution includes the following coupled mechanisms: hydration, ion exchange between alkali or alkaline earth metal ions in glass, and hydrogen species (H^+ , H_3O^+ , and H_2O) in solution²⁶, hydrolysis of ionic-covalent network²⁷, the condensation of dissolved species^{28,29}, and the formation of more stable crystalline phases^{30,31}. In relatively stable conditions, a corrosion layer (or “hydrated”, “ion-depleted”, and “gel”) is easily developed on the glass surface due to the processes of hydration and ion exchange, although there is still no consensus on the formation mechanism^{32–35}. Simultaneously, the process may cause the pH value of the local area to increase and promote the dissolution of the glass network.

The seawater in Fujian has a weakly alkaline environment with a pH of approximately 8.2, and the variance between pH values at different sea depths is negligible³⁶. The average salinity of the seawater was 30.46–31.89‰²². Compared with acidic or neutral solutions, there is greater ion-exchange resistance in this weakly alkaline salt solution, which implies that the silica-network structure of the glass phase is less likely to be broken and dissolved, making it difficult to form a cation-depleted layer on the glaze surface. It may explain why the majority of samples underwent a relatively low degree of chemical corrosion. If the buried conditions of the porcelain remained in a relatively stable state within a certain period, as the concentration of hydrated silica and other dissolved species in the local solution increases, polymerization and supersaturation occur, causing silica nucleation on the hydroxylated glass-surface sites, forming a corrosion layer of amorphous silica spherical aggregates^{37–39}. An interface-coupled glass dissolution–silica reprecipitation mechanism may be used to explain this process³⁷, but the long-term corrosion process in the natural environment is obviously more complicated and fluid³⁸, further study is needed to determine whether this mechanism is suitable for ancient glazes with complex systems.

If the surrounding environment is disturbed, the glaze surface is directly exposed to seawater. With the continuous impact of the sand and other debris particles carried by seawater, more defects could be formed on the glaze surface, such as small pits in Fig. 2c.

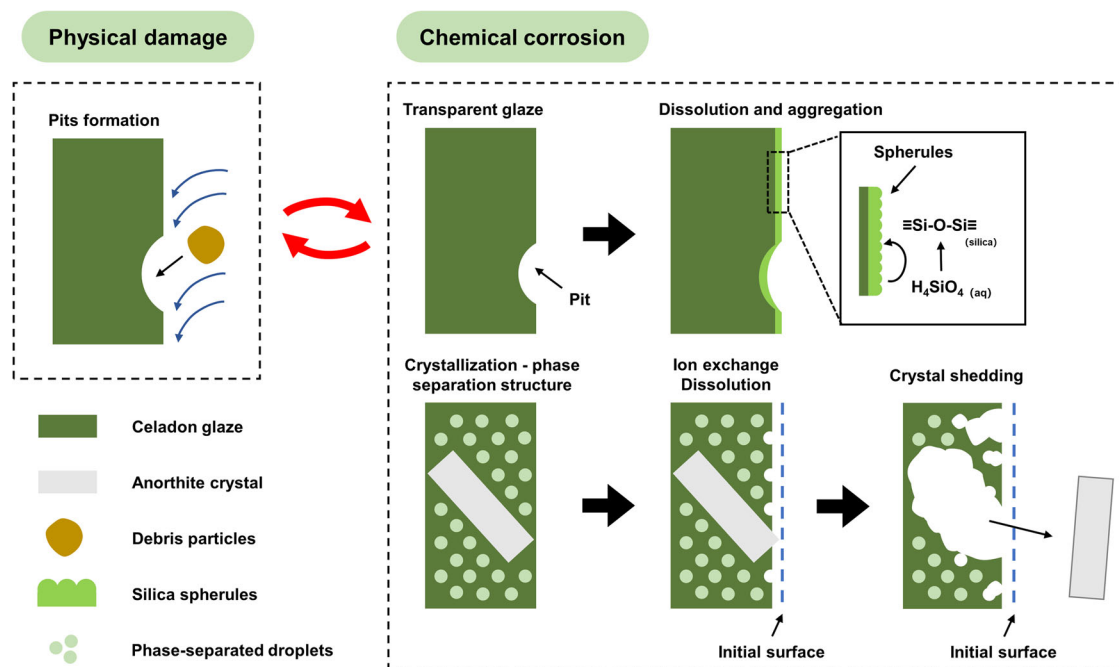


Fig. 4 Schematic of the degradation process of celadon glazes in the marine environment. The red two-way curved arrows indicate the synergistic effects of physical damage and chemical corrosion. The description of each elements is shown in the lower left corner of the figure.

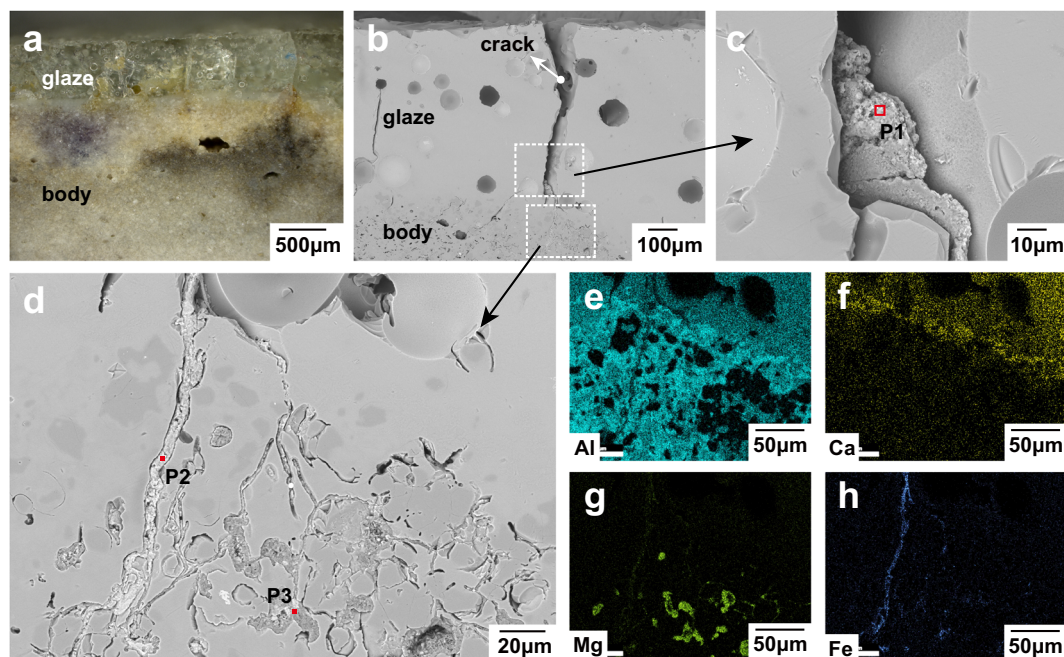


Fig. 5 The contaminants in sample No. 06. **a** and **b** are OM and SEM images of the polished cross section, respectively; **c** yellow substances in a crack: rectangular area in **b**; **d** the contaminants in a crack near glaze-body interface: rectangular area in **b**; **e–h** are the EDS mapping results of **d**.

Table 3. Chemical compositions of the marked positions shown in Fig. 5 (in wt%).

Position No.	C	O	Mg	Al	Si	Ca	Fe
P1	15	41	7	16	10	2	9
P2	12	45	8	16	10		9
P3		44	31	21	4		

The shallow closed pores in the glaze may also be broken, and the original crack network is gradually extended and expanded. These defects provide fast channels for seawater to enter the glaze and larger contact area for chemical corrosion. The microstructure inside the glaze directly exposes and contacts with seawater, thus promoting the progress of corrosion. On the other hand, chemical corrosion can also lead to the break of the glass structure and the formation of microcracks, so it is easier to cause the loss of glaze by the impact of mechanical force. A simplified schematic of the degradation process of the glaze is shown in Fig. 4, demonstrating the combined effect of physical damage and chemical corrosion.

Most of the cracks in No. 06 penetrated the glaze and extended into the body (Fig. 5a and b). There are large areas in the body that are yellow, black, and purple, among other colors, which may be caused by contamination from the external environment. It can be seen in the OM image that the cracks likely provide a channel for the entry of exotic substances. There are some yellow substances (the color is determined by OM) in one of the cracks, with a similar contrast to that of the nearby glaze (in SEM image Fig. 5c). However, the microstructure of the yellow substance in the crack is loose and porous, and the EDS analysis results show (Table 3) that they mainly comprise C, O, Al, Si, Fe, Mg, and a small amount of Ca, indicating that they may have formed during the corrosion process. The crack near the glaze-body interface is filled with substances with higher contrast (Fig. 5d), and the composition resembles the porous substance mentioned above (Table 3). The EDS mapping analysis was repeated at the glaze-body interface area where the color changed, and the results showed

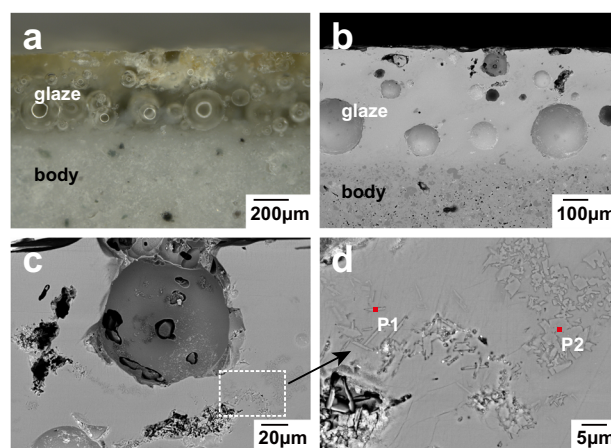


Fig. 6 OM and SEM images of sample No. 07. **a** and **b** are OM and SEM images of the polished cross section, respectively; **c** a bubble and a few irregular shaped holes near the surface; **d** short column-like crystals in the glaze.

that Fe was mainly concentrated in the cracks (Fig. 5h), indicating that Fe is probably from the external environment.

For sample No. 07, most of the glaze layer is clear and transparent and has many bubbles, as shown in the OM and SEM images (Fig. 6a and b). A few irregularly shaped holes were found near the surface. A small number of needle-like or short column-like anorthite crystals were distributed at the glaze-body interface, and short column-like anorthite crystals were also observed near the irregular-shaped holes, as shown in Fig. 6c and d (EDS analysis results are shown in Table 2).

When observed by the naked eye, it was evident that sample No. 07 contained many white spots on the ridges and rim, as well as a deteriorated glaze. The OM and SEM images of the region with white spots are shown in Fig. 7a and b, respectively. It can be observed that there are numerous craters on the glaze surface, and the residual glaze in the craters presents a porous

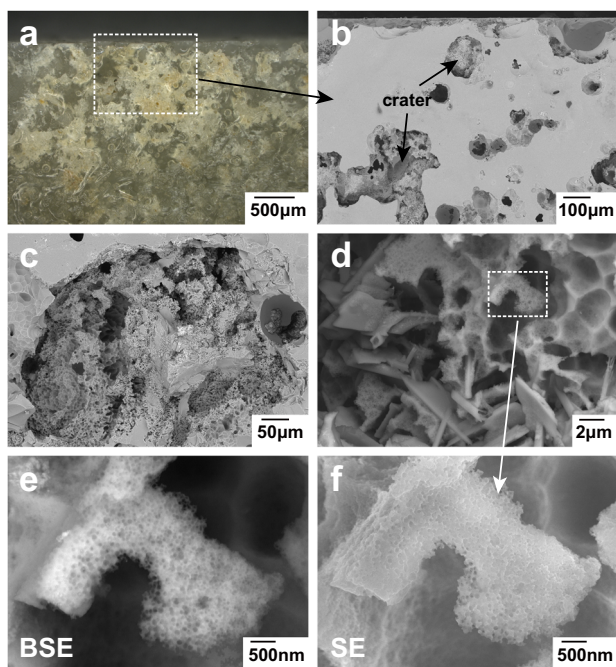


Fig. 7 Corrosion morphology of sample No. 07. **a** and **b** are the OM and SEM images of the seriously corroded region on the glaze surface, respectively; **c** a crater on the glaze surface; **d** the plate-like crystals and nearby phase-separation structure in a crater; **e** and **f** are the framed area in **d**: the porous glass phase, BSE backscattered electron image, SE secondary electron image.

microstructure, as shown in Fig. 7c and d, likely formed after a long period of seawater corrosion. In the magnified SEM images (Fig. 7e and f), densely spaced plate-like crystals and submicron porous microstructures in the surrounding glaze were observed. Although the composition is difficult to acquire because the EDS test signal of the crystal inside the crater was blocked, it can be inferred that these plate-shaped crystals are anorthite, based on the Raman spectrum acquired at the crater position (Supplementary Fig. 7). In addition, the nearby porous microstructure is considered to be a corroded phase-separated structure because previous studies showed that it is always accompanied by anorthite in the ancient Chinese calcium glaze¹⁷. Therefore, the vessel shape of porcelain is also an important consideration. The corrosion state at the ridges and rim of No. 07 is more serious than in other areas, and it has even completely peeled off. The thickness of the glaze at the ridges and rim is often thinner than that of other areas; consequently, it is more likely to be affected by the composition of the body during the firing process to form an anorthite crystal-phase separation structure, which exacerbates the corrosion in these areas (Fig. 7).

Matte glazes

Sample Nos. 08, 09, and 10 were all matte glazes, and they were corroded more severely than the transparent glaze. The XRD diagram of the glaze surface of No. 08 (Fig. 8) shows that the diffraction peaks of quartz, diopside, and anorthite are very prominent. Many long rod-like diopside crystal clusters spread on the glaze surface (Supplementary Fig. 8 and Note 1).

It can be seen in the OM image of the polished cross section (Fig. 9a) that many cracks penetrated the glaze layer and extended into the body. The SEM image (Fig. 9b) shows that in addition to many unmelted quartz grains and bubbles of different sizes, a variety of crystals are densely distributed in the glaze. Figures 9c and e show the magnified SEM images of the glaze-body interface, where there are densely spaced short column-like

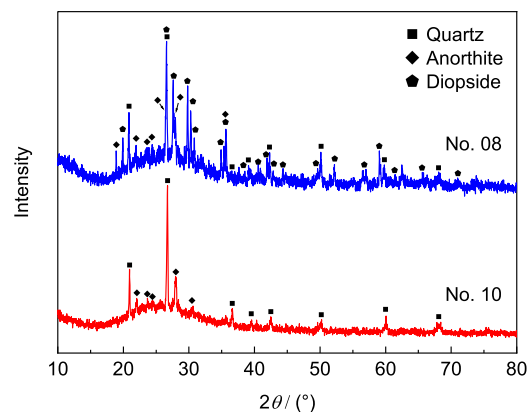


Fig. 8 XRD diagrams acquired on the glaze surface of Nos. 08 and 10. The diffraction peaks of quartz and anorthite exist both in the two samples, while diopside exist only in No. 08.

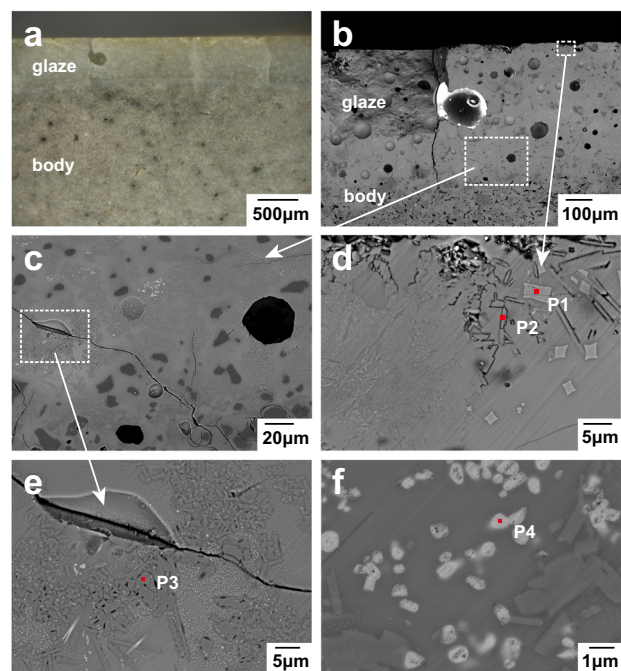


Fig. 9 OM and SEM images of sample No. 08. **a** and **b** are the OM and SEM images of the polished cross section, respectively; **c** and **d** are the magnified SEM images of the glaze-body interface and the area close to the glaze surface, respectively; **e** SEM image of the rectangle region in **c**: short column-like anorthite crystals and phase-separation structure; **f** SEM image of the rectangle region in **d**: crystals with elliptical cross section.

crystals, and the EDS analysis results (Table 2) show a chemical composition compatible with anorthite, which is in agreement with the XRD conclusions. In the area proximal to the glaze surface (Fig. 9d), there are more crystals <10 µm, which have a rhomboid or irregular quadrilateral cross section, in addition to short column-like anorthite crystals. The composition of position P1 in Fig. 9d (the EDS analysis result is in Table 2) is compatible with diopside, supporting the XRD results, indicating that the glazes contain diopside crystals. In addition, a small number of crystals with a high content of P and Ca were found in the glaze (Fig. 9f), which is presented as high-contrast regions in the backscattered electron image. The corrosion morphologies of sample Nos. 08

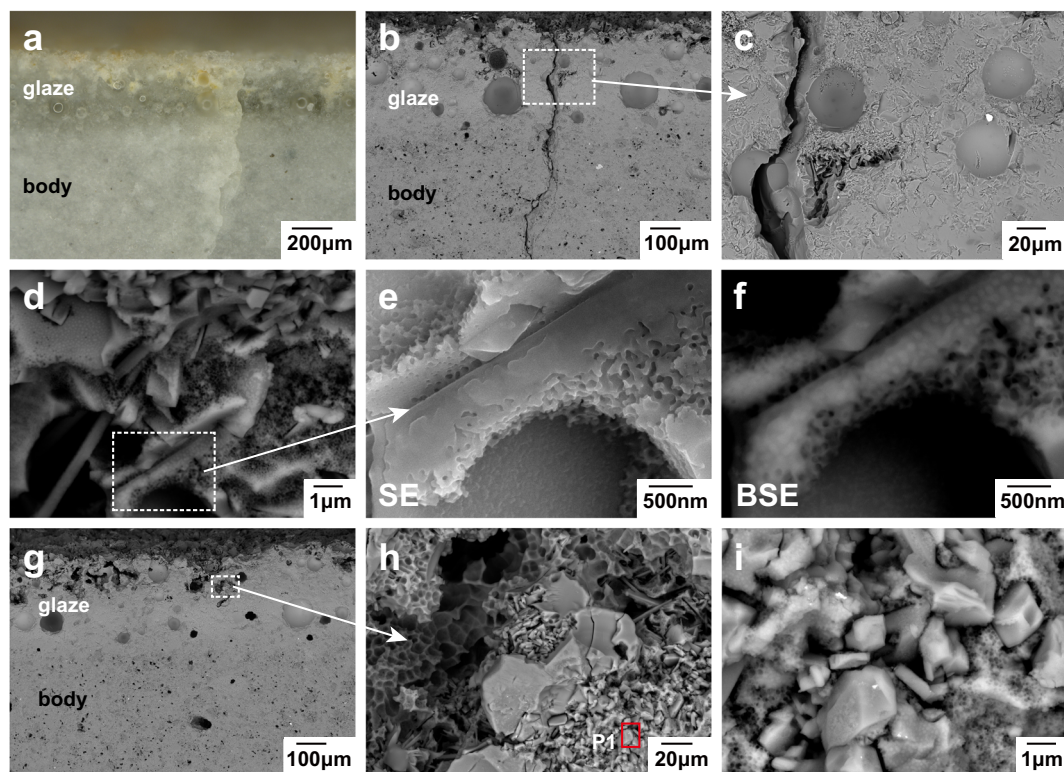


Fig. 10 Corrosion morphology of sample No. 10. **a** and **b** are the OM and SEM images of the polished cross section, respectively; **c** SEM image of the rectangle region in **b**: the corrosion hole near a crack; **d** SEM image of the plate-like crystal in the hole and the corroded glass phase nearby; **e** and **f** are the secondary electron image and backscattered electron image of the porous glass phase in **d**, respectively; **g** SEM image of the polished cross section: the area with many interconnected craters near the glaze surface; **h** SEM image of a crater in the glaze; **i** SEM image of the anorthite crystals and the corroded glass phase nearby in a crater.

and 09 are shown in the supplementary material (Supplementary Fig. 8, Fig. 9, Note 1, and Note 2). Figure 9e and Supplementary Fig. 9c showed that the droplets with higher contrast were dispersed in the matrix. According to previous studies on the crystallization-phase separation structure in the ancient glaze, it can be inferred that the droplet phase and matrix are rich in CaO and SiO₂, respectively^{17,40}. The phase separation structure in the glaze is more prone to corrosion, and many neoformed microstructures, mainly quintinite-group minerals, formed in the cracks and pores of No. 09⁴¹.

Many diopside and anorthite crystals are distributed on the surface and inside of the glaze of Nos. 08 and 09, along with the phase-separated structure. The crystallization-phase-separation structure is a relatively common structural feature in ancient Chinese high-fired calcium glazes, and its formation is simultaneously affected by kinetic factors such as the firing schedule and thermodynamic factors determined by the chemical composition of the glaze^{17,40}. The uneven distribution of these two crystals indicates the complexity and heterogeneity of the glaze microstructure. In terms of chemical composition, the MgO content in the glaze of No. 08 was higher than that of all the transparent glazes (Supplementary Fig. 2) and higher than most Longquan celadon glazes during the Yuan dynasty⁴². Many new microstructures (relative to the pristine glaze microstructure) were formed owing to the serious corrosion of No. 09 under natural conditions, leading to observed changes in the chemical composition, such as the MgO content in the glaze of No. 09 reached 16.31 wt%, while the corrosion of the glaze caused the low SiO₂ content.

From the perspective of physical chemistry, these glazes can be approximately represented by the CaO–MgO–Al₂O₃–SiO₂

quaternary system. When the content of Al₂O₃ was approximately 15 wt%, pyroxene and plagioclase were obtained as the main crystalline phases⁴³. Considering the composition, these Longquan celadon glazes are not fully crystalline, allowing for the formation of a transparent glaze at sufficiently high firing temperatures. During the firing process, the Ca–Mg silicate crystalline phase can be formed at approximately 1000 °C, and with increasing temperature, the crystals gradually melt⁴⁴. However, the firing temperatures of Nos. 08 and 09 are only 1215 °C and 1190 °C (Supplementary Table 3), which are significantly lower than those of Nos. 04 and 06 (1245 °C and 1265 °C, respectively), and they exhibit transparent glazes. The lower firing temperature kept the pyroxene and feldspar crystals precipitated during the heating process without being completely melted. At the same time, the crystallization during the heating process is also reflected in the uneven distribution of crystals in the glaze. Therefore, chemical composition and firing schedule together affected the microstructure of matte glazes. This type of celadon ware with a matte glaze was not deliberately made by the kiln workers but was more likely to be low-quality products that appeared in the mass-production process. Although they retained market value in overseas trade, the selection of raw materials and the control of the firing process were not refined.

The glaze of No. 10, with poor transparency, was seriously corroded, and it contained many white spots, as observed from OM (Fig. 10a). The SEM image of the polished cross section (Fig. 10b and c) shows a crack and a nearby hole in the glaze, in which there are densely spaced plate-like crystals (Fig. 10d). The glass phase around the crystal was corroded, exhibiting a porous microstructure. It can be observed by comparing the secondary electron image (Fig. 10e) and the backscattered electron image

(Fig. 10f) that the phase-separated droplets with higher contrast were corroded to form a porous microstructure. In another position, there are many interconnected craters near the glaze surface (Fig. 10g), in which many anorthite crystals (EDS result is listed in Table 2 and Raman spectrum is shown in Supplementary Fig. 7) and porous microstructures, left by the nearby phase-separated droplets being corroded, can be discovered (Fig. 10h and i). The corrosion microstructure inside the glaze layer also reflects the role of cracks in the corrosion process. The cracks provided a fast channel for seawater to enter the glaze, thereby accelerating the corrosion process.

From the perspective of microstructure, the matte glaze in Longquan celadon is more complicated. Many crystalline phases and phase-separated structures could also have a significant impact on the corrosion process. Therefore, one cannot only focus on the corrosion of the glass phase in the glaze. As shown in Supplementary Fig. 9, Fig. 9e, and Fig. 10f, the CaO-rich droplet phase with higher contrast was dispersed in the SiO₂-rich matrix with lower contrast in the glazes of Nos. 08, 09, and 10. More nonbridging oxygen atoms in the CaO-rich phase made the silica-network structure more open and unstable, so it was more likely to be corroded by seawater. The dissolution of the CaO-rich droplets caused the formation of a porous microstructure, leading to an increase in the local specific surface area and resulted in more seawater entering into the local submicron pores, accelerating the disintegration of the SiO₂-rich continuous phase⁴¹. Finally, many large craters with a size of tens of microns were formed with the shedding of the anorthite crystals, which seriously damaged the esthetics of glaze. A schematic of the process is shown in Fig. 4. In addition, a large number of diopside crystals on the surface of the glaze did not seem to be severely corroded (Supplementary Fig. 8), which may be attributed to its good chemical stability⁴⁵. It is worth noting that the glazes with a large number of crystals such as Nos. 08 and 09 are similar in microstructure to glass ceramics, all of which belong to the multiphase systems, despite the difference in crystal size and homogeneity. The glass-ceramic system is considered to have unique advantages in immobilizing radioactive fission products for long-term disposal, but the multiphase system also makes it more difficult to study the corrosion resistance^{46,47}. This type of ancient glaze may be used as an archeological analog to study the long-term corrosion behavior of multiphase systems in natural environments. Within our study, the results indicate that phases with poor chemical stability are more likely to be preferentially corroded.

Furthermore, the corrosion of porcelain occurs not only in the glaze but also in the body. The body of ancient porcelain in China is mainly composed of crystalline phases such as quartz and mullite, as well as a glass phase and a small number of pores^{16,48}. They can also be corroded under the reaction of prolonged exposure to seawater. On the one hand, the cracks penetrating the glaze layer extended into the body, so the seawater could directly enter the inside of the body, bringing in external species and forming new substances during the corrosion process (Fig. 5g); however, the body may be directly exposed to the external marine environment when porcelain wares are shattered or the glaze is completely corroded, providing different corrosion paths, as shown in Supplementary Fig. 10.

In conclusion, this study yielded insights into the degradation process of several ancient glazes with similar compositions but different microstructures under the same conditions and discussed several factors that affect the long-term degradation behavior of the glazes in the marine environment. Based on a comparative analysis of the different samples, the following conclusions were obtained: (1) the chemical composition of ancient porcelain glazes may change after long-term corrosion in a marine environment, reflecting the alteration of the pristine microstructure and the formation of new microstructures; (2) the

formation of a large number of crystals in the matte glaze is related to the composition and the lower firing temperature; (3) the degradation of the glazes is affected by the physical damage as well as the chemical corrosion. Due to the severe physical damage, the glaze surface became rough and lackluster, which also promoted the chemical corrosion process. The combined effect of them may lead to more severe degradation. (4) The transparent glaze mainly experienced the process of dissolution and reprecipitation, resulting in the formation of a corrosion layer of spherical aggregates; (5) the severe corrosion of the matte glaze resulted from the lower chemical stability of the anorthite crystallization-phase-separation structure. Among them, the CaO-rich droplet phase and the crystal-glass interface layer dissolved more easily and were preferentially corroded in the marine environment; (6) the corrosion process of porcelain in the marine environment is affected by internal factors, such as the glaze composition, microstructure, and shape of the ware, in addition to external environmental factors.

METHODS

Analytical techniques

The chemical compositions of the bodies and glazes were quantitatively examined using EDXRF (energy-dispersive X-ray fluorescence, Bruker M4 TORNADO). The body was tested on a polished cross section, and the glaze was tested on both the natural surface and polished cross section. Bruker M4 TORNADO was equipped with a 30-W (50 V, 600 μ A) X-ray tube, and the diameter of the X-ray focus was 25 μ m. For quantitative analysis, the calibration process involved several steps. First, a series of 13 standard samples was formulated using standard geological minerals. Calibration curves were created for each element in the standard series, representing the relationship between the intensity of the element characteristic peak and the element concentration. The EDXRF data were calibrated according to the calibration curves. Analysis was carried out using the software accompanying the instrument.

X-ray diffraction (Bruker D8 DISCOVER) using Cu K α radiation (40 kV, 40 mA) was applied to investigate the phase components of the glaze surface. Analyses were performed directly on the surface of the fragments.

Macroscale morphologies of the glaze surfaces and polished cross sections were observed using an optical microscope (Keyence VHX-2000). The micromorphology and semiquantitative microarea chemical compositions of the glaze surface and polished cross section of the samples were characterized using field-emission scanning electron microscope (FEI Magellan400) equipped with EDS. Before the SEM-EDS analysis, the samples were coated with platinum (for No. 06) or carbon (for all other samples).

The firing temperature of the body was measured using a dilatometer (NETZSCH DIL 402C). To prepare the test samples, the glazes were grounded, and the bodies were cut into pieces of 5 \times 5 \times 25 mm³. Due to sample-size limitation, only some of the samples that met the requirements were tested. The heating rate of the dilatometer was 5 $^{\circ}$ C/min, and the approximate value of the firing temperature of the sample was obtained according to the inflection point in the thermal expansion curve^{49,50}. The firing-temperature results are listed in Supplementary Table 3.

Micro-Raman spectroscopy (Horiba XploRA one) was applied to examine the glaze on both the natural surface and polished cross sections. The Raman spectral signal was recorded from 100 cm⁻¹ to 3500 cm⁻¹, using a 532 nm excitation radiation source (25 mW). For glass phase, each Raman spectrum was acquired in 10 accumulation cycles, and the integration time for each one is 20 s. The wavenumber calibration of the peak position was at a \times 50 objective with a piece of crystal silicon. A confocal microscope (Olympus BX41) was employed to focus the laser beam on the test areas with \times 10 and \times 50 objectives. The baseline was subtracted using the LABSPEC software, and the smooth deconvolution of the spectra was performed using the Origin software^{51,52}.

Celadon samples

In this study, 11 typical celadon shards with varying degrees of degradation from the Dalian Island shipwreck of the Yuan Dynasty, provided by the Fujian Museum, were investigated. The samples were immersed in deionized water for desalination after the excavation.

The bodies of 11 samples were all gray, and the glaze colors were green or yellow-green. There are large discrepancies in appearance and preservation of the samples, which can be divided into four categories: bright as new (Nos. 01–05), lacking luster (Nos. 06 and 07), a matte glaze (Nos. 08–10), and underfired (No. 11). Sample photos, appearance descriptions, and the analysis results of the firing temperatures are listed in Supplementary Table 3.

DATA AVAILABILITY

The datasets generated during and/or analyzed during the current study are available from the corresponding author on reasonable request.

Received: 29 April 2021; Accepted: 27 December 2021;

Published online: 21 January 2022

REFERENCES

- Frankel, G. S. et al. A comparative review of the aqueous corrosion of glasses, crystalline ceramics, and metals. *NPJ Mater. Degrad.* **2**, 15 (2018).
- Frankel, G. S. et al. Recent advances in corrosion science applicable to disposal of high-level nuclear waste. *Chem. Rev.* **121**, 12327–12383 (2021).
- Gin, S., Delaye, J.-M., Angeli, F. & Schuller, S. Aqueous alteration of silicate glass: state of knowledge and perspectives. *NPJ Mater. Degrad.* **5**, 42 (2021).
- Majérus, O. et al. Glass alteration in atmospheric conditions: crossing perspectives from cultural heritage, glass industry, and nuclear waste management. *NPJ Mater. Degrad.* **4**, 27 (2020).
- Pearson, C. *Conservation of Marine Archaeological Objects* (Butterworths, 1987).
- Clark, D. E., Zaitos, B. K. *Corrosion of Glass, Ceramics and Ceramic Superconductors* (Noyes Publications, 1992).
- Hao, X., Zhu, T., Xu, J., Wang, Y. & Zhang, X. Microscopic study on the concretion of ceramics in the “Nanhai I” shipwreck of China, Southern Song Dynasty (1,127–1,279 A.D.). *Microsc. Res. Tech.* **81**, 486–493 (2018).
- Du, J., Luo, W., Li, N. & Wang, C. Characterization of the micro-contaminants from the inner-body of Kraak porcelain excavated from the “Nan’ao I” shipwreck, the South China Sea. *Herit. Sci.* **7**, 85 (2019).
- Hu, X. Conservation study on pieces of marine porcelain found at the Hua Guang Jiao No. 1 shipwreck site in Xisha. *Sci. Conserv. Archaeol.* **25**, 54–64 (2013).
- Ma, Y. Preliminary study on the desalination protection of ceramics excavated underwater in China. *Mus. Res.* **97**, 85–89 (2007).
- Huang, S. Desalination treatment and reinforcement protection of porcelain excavated underwater. *Fujian Wenbo* **4**, 90–93 (2012).
- Chen, Y., Li, N., Luo, W. & Wang, C. A study on method of desalination of ceramics from the Huaguangjiao I shipwreck. *Jiangnan Archaeol.* **126**, 117–122 (2013).
- Xi, A. Comparative study on desalination technology of ceramic wares excavated from “Nan’ao I”. *Sci. Conserv. Archaeol.* **32**, 90–97 (2020).
- Li, W., Chen, Y., Li, N., Li, B. & Luo, W. A study on quantitative evaluation of damage in conservation of ceramics from Huaguangjiao I shipwreck with ICP-AES. *Spectrosc. Spectr. Anal.* **35**, 772–776 (2015).
- Huang, H., Yang, Q. & Wu, L. Safety evaluation of micro-nano bubble cleaning for underwater porcelain from Nanhai I shipwreck. *Sci. Conserv. Archaeol.* **29**, 30–37 (2017).
- Zhang, F. *The Science of Chinese Ancient Ceramics* (Shanghai People’s Fine Arts Publishing House, 2000).
- Li, W. Glazes in China. In *Encyclopaedia of the History of Science, Technology, and Medicine in Non-Western Cultures* (Ed. Selin, H.) 2113–2124 (Springer Reference, 2015).
- Li, G. et al. Aging study on the modern imitation glaze and ancient glaze of the Ming and Qing dynasties based on FTIR decomposition spectra. *J. Non Cryst. Solids* **505**, 102–108 (2019).
- Kirmizli, B., Chen, S. & Colomban, P. The Raman signature of protonic species as a potential tool for dating or authentication of glazed pottery. *J. Raman Spectrosc.* **50**, 696–710 (2019).
- Ma, Q., Xu, S., Wang, J. & Yan, J. Integrated analysis of a black-glazed porcelain bowl in Tushan Kiln dated back to Song Dynasty, China. *Mater. Chem. Phys.* **242**, 122213 (2019).
- Li, Z., Ma, Y., Ma, Q., Chen, J. & Song, Y. New perspective on Jun glaze corrosion: study on the corrosion of light greenish blue and reddish purple glazes from Juntai Kiln, Yuzhou, Henan, China. *Herit. Sci.* **8**, 2 (2020).
- Underwater Archaeological Research Center of National Museum of China, Institute of Cultural Relics and Archaeology of Fujian Museum, Fuzhou Archaeological team. *The Yuan Dynasty Shipwreck Site at Dalian Island, Fujian Pingtan* (Science Press, 2014).
- Li, J. *History of Science and Technology in China: Ceramic Volume* (Science Press, 1998).
- Colomban, P. & Paulsen, O. Non-destructive determination of the structure and composition of glazes by Raman spectroscopy. *J. Am. Ceram. Soc.* **88**, 390–395 (2005).
- De Ferri, L. et al. Raman study of model glass with medieval compositions: artificial weathering and comparison with ancient samples. *J. Raman Spectrosc.* **43**, 1817–1823 (2012).
- Doremus, R. H. Interdiffusion of hydrogen and alkali ions in a glass surface. *J. Non Cryst. Solids* **19**, 137–144 (1975).
- Hench, L. L. & Clark, D. E. Physical chemistry of glass surfaces. *J. Non Cryst. Solids* **28**, 83–105 (1978).
- Lombardo et al. Characterisation of complex alteration layers in medieval glasses. *Corros. Sci.* **72**, 10–19 (2013).
- De Ferri, L., Lottici, P. P. & Vezzalini, G. Characterization of alteration phases on Potash–Lime–Silica glass. *Corros. Sci.* **80**, 434–441 (2014).
- Aréna, H. et al. Impact of iron and magnesium on glass alteration: characterization of the secondary phases and determination of their solubility constants. *Appl. Geochem.* **82**, 119–133 (2017).
- Frugier, P. et al. SON68 nuclear glass dissolution kinetics: Current state of knowledge and basis of the new GRAAL model. *J. Nucl. Mater.* **380**, 8–21 (2008).
- Douglas, R. W. & El-Shamy, T. M. M. Reactions of glasses with aqueous solutions. *J. Am. Ceram. Soc.* **50**, 1–8 (1967).
- Advocat, T., Crovisier, J. L., Vernaz, E., Ehret, G. & Charpentier, H. Hydrolysis of R7T7 nuclear waste glass in dilute media: mechanisms and rate as a function of pH. *MRS Proc.* **212**, 57 (1990).
- Gong, Y., Xu, J. & Buchanan, R. C. The aqueous corrosion of nuclear waste glasses revisited: probing the surface and interfacial phenomena. *Corros. Sci.* **143**, 65–75 (2018).
- Conradt, R. Chemical durability of oxide glasses in aqueous solutions: a review. *J. Am. Ceram. Soc.* **91**, 728–735 (2008).
- Lei, Z. *Environment Manual of China Sea* (Shanghai Jiao Tong University Press, 1988).
- Geisler, T. et al. The mechanism of borosilicate glass corrosion revisited. *Geochim. Cosmochim. Acta* **158**, 112–129 (2015).
- Dohmen, L. et al. Pattern formation in silicate glass corrosion zones. *Int. J. Appl. Glass Sci.* **4**, 357–370 (2013).
- Gin, S. et al. A general mechanism for gel layer formation on borosilicate glass under aqueous corrosion. *J. Phys. Chem. C* **124**, 5132–5144 (2020).
- Li, W., Li, J., Deng, Z., Wu, J. & Guo, J. Study on Ru ware glaze of the Northern Song dynasty: One of the earliest crystalline-phase separated glazes in ancient China. *Ceram. Int.* **31**, 487–494 (2005).
- He, Y., Li, W., Li, J., Xu, C. & Lu, X. Corrosion of Longquan celadons in the marine environment: study on the celadons from the Dalian Island shipwreck of the Yuan Dynasty. *Herit. Sci.* **9**, 104 (2021).
- Ding, Y. et al. The body glazes of the Song-Yuan-Ming Longquan celadon products and their sintered temperature. *Palace Mus. J.* **7**, 33–41 (2019).
- Huang, R. Chen, X. Chen, S. Guo, R. Study on Tang Dynasty tea dust porcelain, in: *“Science and Technology of Ancient Ceramics.” Proceedings of the 1992 International Symposium* (eds Li, J. Chen X.) 144–154 (Shanghai Scientific and Technological Literature Press, 1992).
- Chen, X., Chen, S., Zhou, X., Guo, R. & Sun, H. The study on Jin and Yuan Dynasties tea dust wares from Xunyi kiln site. *J. Ceram.* **17**, 15–24 (1996).
- Fröberg, L., Kronberg, T., Törnblom, S. & Hupa, L. Chemical durability of glazed surfaces. *J. Eur. Ceram. Soc.* **27**, 1811–1816 (2007).
- Neeway, J. J. et al. Kinetics of oxyapatite [Ca₂Nd₈(SiO₄)₆O₂] and powellite [(Ca,Sr,Ba)MoO₄] dissolution in glass-ceramic nuclear waste forms in acidic, neutral, and alkaline conditions. *J. Nucl. Mater.* **515**, 227–237 (2019).
- Matthew Asmussen, R., Neeway, J. J., Kaspar, T. C. & Crum, J. V. Corrosion behavior and microstructure influence of glass-ceramic nuclear waste forms. *Corrosion* **73**, 1306–1319 (2017).
- Tite, M. S., Freestone, I. C. & Wood, N. An investigation into the relationship between the raw materials used in the production of Chinese porcelain and stoneware bodies and the resulting microstructures*. *Archaeometry* **54**, 37–55 (2012).
- Tite, M. S. Determination of the firing temperature of ancient ceramics by measurement of thermal expansion. *Nature* **222**, 81–81 (1969).
- Lu, X., Xu, C. & Li, W. Applied research on the push-rod thermal expansion method used to determine firing temperatures of ancient ceramics. *Sci. Conserv. Archaeol.* **32**, 70–80 (2020).
- Colomban, P. Polymerization degree and Raman identification of ancient glasses used for jewelry, ceramic enamels and mosaics. *J. Non Cryst. Solids* **323**, 180–187 (2003).
- Colomban, P., Tournie, A. & Bellot-Gurlet, L. Raman identification of glassy silicates in ceramics, glass and jewellery: a tentative differentiation guide. *J. Raman Spectrosc.* **37**, 841–852 (2006).

ACKNOWLEDGEMENTS

This work was supported by National Key R&D Program of China [2019YFC1520205, 2019YFC1520202] and National Natural Science Foundation General Program of China [51672302].

AUTHOR CONTRIBUTIONS

W.L. conceived the experimental research, and was responsible for funding acquisition, writing—review and editing. Y.H. performed the data analysis and wrote the paper. J.L. provided the celadon samples. C.X and X.L. contributed to the experiments. Everyone participated in discussions and analysis of the results.

COMPETING INTERESTS

The authors declare no competing interests.

ADDITIONAL INFORMATION

Supplementary information The online version contains supplementary material available at <https://doi.org/10.1038/s41529-022-00217-5>.

Correspondence and requests for materials should be addressed to Weidong Li.

Reprints and permission information is available at <http://www.nature.com/reprints>

Publisher's note Springer Nature remains neutral with regard to jurisdictional claims in published maps and institutional affiliations.



Open Access This article is licensed under a Creative Commons Attribution 4.0 International License, which permits use, sharing, adaptation, distribution and reproduction in any medium or format, as long as you give appropriate credit to the original author(s) and the source, provide a link to the Creative Commons license, and indicate if changes were made. The images or other third party material in this article are included in the article's Creative Commons license, unless indicated otherwise in a credit line to the material. If material is not included in the article's Creative Commons license and your intended use is not permitted by statutory regulation or exceeds the permitted use, you will need to obtain permission directly from the copyright holder. To view a copy of this license, visit <http://creativecommons.org/licenses/by/4.0/>.

© The Author(s) 2022